Design of non-equiatomic high entropy alloys with heterogeneous lamella structure towards strength-ductility synergy

Article *in* Scripta Materialia · May 2018

DOI: 10.1016/j.scriptamat.2018.05.020

CITATIONS
2

READS
124

4 authors, including:

Cheng Zhang
University of California, San Diego
4 PUBLICATIONS **23** CITATIONS
SEE PROFILE

Chaoyi Zhu
University of California, San Diego
6 PUBLICATIONS **12** CITATIONS
SEE PROFILE

Kenneth S. Vecchio
University of California, San Diego
220 PUBLICATIONS **6,403** CITATIONS
SEE PROFILE

Scripta Materialia 154 (2018) 78–82

Contents lists available at ScienceDirect

Scripta Materialia

journal homepage: www.elsevier.com/locate/scriptamat

Regular article

Design of non-equiatomic high entropy alloys with heterogeneous lamella structure towards strength-ductility synergy

Cheng Zhang [a], Chaoyi Zhu [a], Tyler Harrington [a], Kenneth Vecchio [a,b,*]

[a] Materials Science and Engineering Program, University of California San Diego, La Jolla, CA 92093-0448, USA
[b] Department of NanoEngineering, University of California San Diego, La Jolla, CA 92093-0448, USA

ARTICLE INFO

Article history:
Received 7 April 2018
Received in revised form 15 May 2018
Accepted 16 May 2018
Available online xxxx

Keywords:
Heterogeneous lamella
High entropy alloy
Non-equiatomic
NCACB

ABSTRACT

A non-equiatomic FeNiCoAlCrB (NCACB) high entropy alloy (HEA) with a heterogeneous lamella (HL) structure is fabricated through conventional thermomechanical processing. In the HL microstructure, fine-grain regions result from inhibited grain growth due to Zener pinning of boundaries by NiAl (B2) precipitates, while coarse-grained regions originate from grain growth within large deformation bands in the absence of precipitates. A back-stress strengthening mechanism, unique to deformation of heterogeneous microstructures, is verified through mechanical behavior and electron backscatter diffraction enabled geometrically necessary dislocation density analysis. This mechanism gives rise to the combination of both high strength and high ductility in HL-NCACB-HEA.

Owing to attractive engineering properties, high entropy alloys (HEAs) have drawn great attention over the past decade [1–5]. During this time of exploration, most studies have been focused on one of the original concepts of HEAs for alloy design, which utilizes an equiatomic ratio of multiple principal elements to obtain the maximum configurational entropy [1]. However, this design concept limits the compositional space and excludes non-equiatomic candidates with potentially outstanding properties and more commercially viable. The concept of non-equiatomic HEAs, first put forward by Raabe and his colleagues [6–10], has greatly expanded the compositional space for HEA design, and work on these compositions has achieved unparalleled mechanical properties [6]. On the other hand, in the development of traditional metals and alloys, modification of mechanical properties through controlled microstructure design has succeeded in many studies. Heterogeneous lamella structures, bimodal structures, and gradient structures have been fabricated in pure Ti/Cu, steels and aluminum alloys over a wide range of length scales to overcome the strength-ductility trade-off [11–22]. For the fabrication of these microstructures, powder metallurgy with different size particles, surface mechanical attrition treatment (SMAT) techniques and asymmetrical rolling with subsequent annealing are typically employed [11–22]. Nevertheless, to these authors' knowledge, an effective method for the fabrication of a heterogeneous lamella structure in non-equiatomic HEAs has never been reported. In this study, a method using precipitation (NiAl) controlled development of non-equiatomic HEAs with heterogeneous lamella structure has been devised. It is a reliable and reproducible method to manufacture a novel, heterogeneous lamella, non-equiatomic, $Fe_{34.95}Ni_{27.5}Co_{17.5}Al_{11.5}Cr_{8.5}B_{0.05}$ (at.%) (NCACB) HEA with high strength and high ductility. This composition can be regarded as a non-equiatomic HEA because the composition is clearly non-equiatomic, but has a Valence Electron Configuration (VEC) value of 8.0 (in the range of FCC-HEA, $7.5 < VEC < 9.5$) [23], has a mixing enthalpy (ΔH) of −8.5 kJ/mol (in the range of HEA, $-15\ kJ/mol < \Delta H < 5\ kJ/mol$) [24], and has a configurational entropy (ΔS) value of 1.52R [1].

NCACB ingots were prepared through arc-melting under an argon atmosphere with raw materials as follows: Fe (99.95%), Ni (99.9%), Co (99.9%), Al (99.9%), Cr (99.9%), and Ni_2B (99%). Each ingot was flipped and re-melted eight times to ensure homogeneity. Next, each NCACB ingot with an original thickness of ~10 mm was processed through homogenization (1300 °C, 3 h), hot rolling (1250 °C, reduction in thickness (RIT) of ~30%), cold rolling (RIT ~ 90%), annealing at 1000–1300 °C for various times and water quenched. Depending on the annealing conditions, distinct microstructures can be achieved, e.g. fine grain (FG), coarse grain (CG) and heterogeneous lamella (HL) microstructures.

Microstructure characterization was performed in a Thermo-Fisher (formerly FEI) Apreo FEG-SEM equipped with Oxford Instruments EDS and EBSD-Symmetry detectors. Thin samples rolled to a RIT = 90% were cut to standard dog-bone tensile shapes, and metallographic samples were ground and polished using standard metallographic techniques, followed by vibratory polishing. Quasi-static tensile tests were carried out at room temperature, with the tensile direction parallel to the rolling direction [gauge dimensions: 20 × 2 × 0.5 (mm)]. After

* Corresponding author at: Department of NanoEngineering, University of California San Diego, 9500 Gilman Dr., MC-0448, La Jolla, CA 92093-0448, USA.
E-mail address: kvecchio@eng.ucsd.edu (K. Vecchio).

https://doi.org/10.1016/j.scriptamat.2018.05.020
1359-6462/

tensile tests, the geometrically necessary dislocation (GND) density in the deformed HL NCACB was calculated from EBSD orientation data using an in-house Matlab code developed by Zhu et al. [25,26].

Fig. 1(A) shows the large deformation bands found in NCACB after cold rolling to a RIT of 90%. These deformation bands were previously reported in cold rolling (RIT = 90%) of polycrystalline nickel with an initial average grain size of 500 μm [27], but were not formed when the initial average grain size was between 80 and 100 μm [28]. Hence, we conclude that each observable deformation band corresponds to one initial large grain in the NCACB sample prior to cold rolling (refer to Supplementary Figs. S1 and S2 for the microstructure evolution prior to cold rolling). Similar phenomena have been observed in aluminum alloys with different grain sizes at large strains [29–31]. As for small grains, microbands are found across the entire microstructure [28,29,31–33], which leads to subdivision of grains instead of the formation of large deformation bands. Overall, highly heterogeneous deformation during cold rolling leads to subdivision of small grains with NiAl particles along sub-grain/grain boundaries, and elongation of large grains into deformation bands. The unique heterogeneous microstructure for NCACB over a large region is shown in Fig. 1(B) & (C) after annealing at 1150 °C for 1 h after a RIT of 90% in the cold rolling step. At higher magnifications, coarse and fine grains are present in bands as more clearly shown in (Supplementary Figs. S3(A) & S5(B)). Fine grain and coarse grain regions differ in size by almost three to four orders of magnitude (Supplementary Fig. S3(B)), therefore this alloy is referred to as HL (heterogeneous lamella microstructure)-HEA (type of alloy)-1150 (annealing temperature). This microstructure was reproduced consistently under these processing conditions and is not a unique anomaly.

To understand the formation mechanism of the heterogeneous lamella (HL) structure, a microstructure evolution study of NCACB through a series of heat-treatment conditions was undertaken. While secondary phase precipitates are observed along the boundaries of fine grains that are composed of Ni and Al according to EDS analysis (Fig. 2(B)), no secondary phase is found along the grain boundaries in the coarse-grained regions. Combined EDS mapping and XRD in Fig. 2 further confirm that these particles are NiAl (B2) β phase particles embedded in a matrix of the γ (FCC) phase. Therefore, NiAl precipitates are formed prior to the heat treatment since no additional NiAl has precipitated out along coarse grain boundaries during the annealing step at 1150 °C. Consequently, large deformed bands preferably grow into a coarse-grained region as grain boundaries quickly sweep across the deform band without resistance from particle pinning. SEM images of NCACB (CR90, 1150 °C 60-min) at different magnifications are shown in Supplementary Fig. S4(A), which clearly indicate the presence of the HL structure. Small NiAl precipitates distributed outside the large deformation bands not only act as the nuclei for the recrystallization [34,35], but also suppress grain growth due to Zener pinning of the boundaries (detailed calculation can be found in the Supplementary material). As the temperature is further increased to 1200 °C, no NiAl precipitates are observed along grain boundaries for an annealing time of 10 min, (Supplementary Fig. S4(E3)), indicating that these B2 particles are completely dissolved into the γ matrix. However, NCACB annealed at 1000 °C for 1 h, as shown in Supplementary Fig. S2(F), does not exhibit the HL structure. As NiAl particles precipitate out within large deformation bands at 1000 °C, the pinning effect restricts grain growth over the entire sample to produce a fine grain microstructure with an average grain size of 4.7 μm, hence the term: FG-HEA-1000. Based on the above study on annealing conditions, 1150 °C is a temperature low enough to prevent NiAl outside deformation bands from dissolving into the matrix, and yet high enough to suppress precipitation within large deformation bands. Consequently, this condition leads to fast grain growth within the large deformation bands and suppression of grain growth outside the large deformation bands, i.e. formation of heterogeneous lamella structure in NCACB-HEA.

Fig. 3(A)–(C) shows tensile properties of four NCACB with distinct microstructures, and the comparison between NCACB-HEA and other existing materials. The microstructures of these four NCACB samples are presented in Supplementary Fig. S5(A)–(D): FG-HEA-1000 with average grain size of 4.7 μm, HL-HEA-1150, CG-HEA-1200 with average grain size of 140 μm, and CG-HEA-1300 with average grain size of 400 μm. In Fig. 3(A), HL-HEA-1150 sample can achieve an ultimate tensile strength (UTS) of 690 MPa with total elongation of 34%, which gives the best combination of strength and ductility. The ultra-high ductility in CG-HEA 1300 is due to the relatively large grain size (grain size/thickness) and strong texture that lead to the formation of a bamboo-like or oligocrystal structure, which effectively reduces the grain constraint and the deformation mimics that of a single crystal [36–40]. On the other hand, CG-HEA-1200 undergoes significant heterogeneous deformation as misfit strains of differently orientated grain (random texture) induce plastic strain gradients as well as residual stresses, hence lower ductility. The ultra-high strength in FG-HEA 1000 can be attributed to smaller grain size, i.e. Hall-Petch effect and presence of larger fraction of precipitates, i.e. precipitation strengthening; the latter of which compromises the overall ductility of the material. In comparison with CG-HEA-1200, whose grain size is close to those in the coarse-grained bands of HL-HEA-1150, the HL sample shows nearly twice the UTS, while maintaining the same ductility. When comparing with FG-HEA-1000, the HL sample exhibits slightly lower strength, with significantly enhanced ductility. Moreover, Fig. 3(B)–(C) includes true stress-strain curves and strain hardening rate curves for these four NCACB samples, which shows significant strain hardening in HL and FG samples. In Fig. 3(D), some metals fabricated through microstructure design are presented here for comparison to this work in the UTS versus total elongation plot. Many of these materials compromise either ductility or strength to achieve their target properties. By comparison, the mechanical properties of NCACB-HEA can be better tuned through the

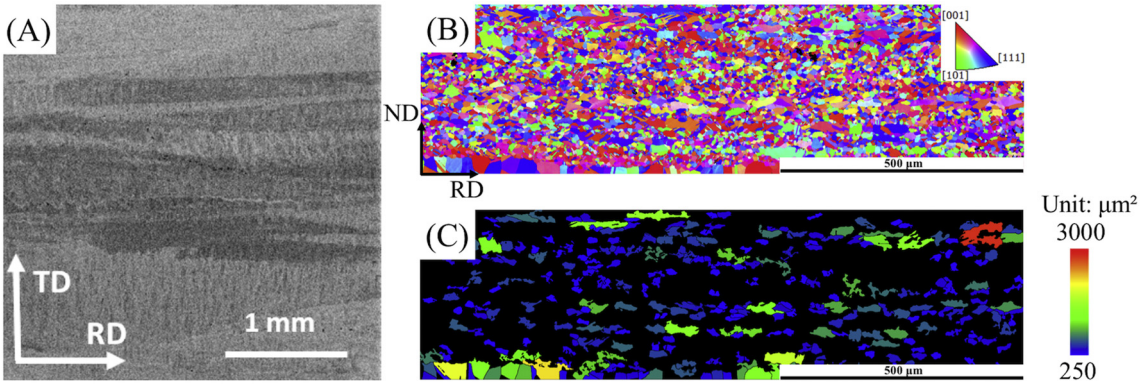

Fig. 1. (A) SEM (BSE) image for NCACB after cold rolling (RIT = 90%), RD-rolling direction, TD-transverse direction; (B) EBSD IPFX map for NCACB in the transverse direction after annealing at 1150 °C for 1 h; (C) grain area map corresponding to (B).

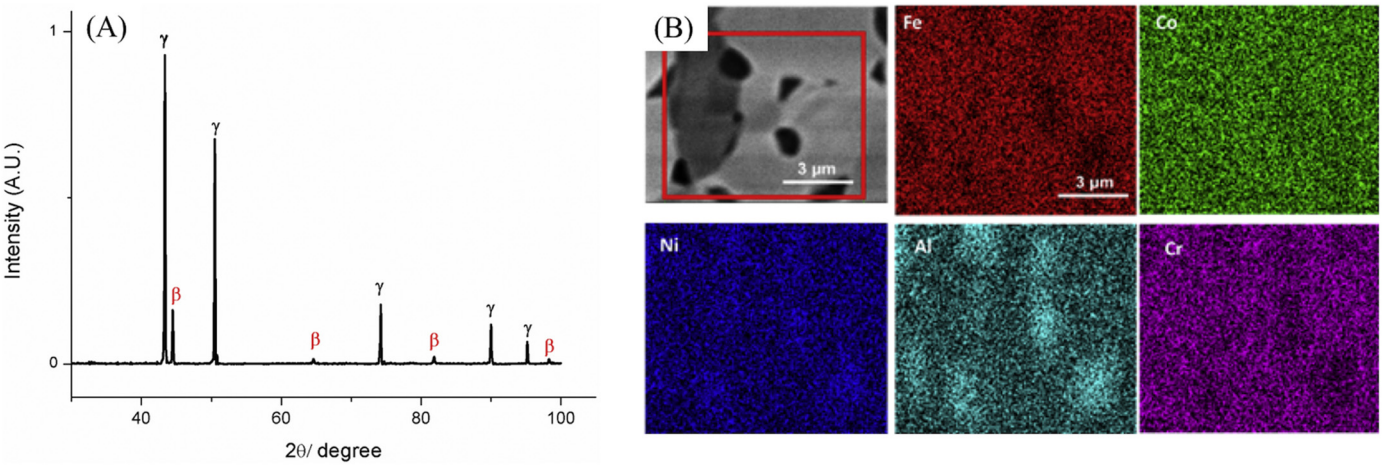

Fig. 2. (A) XRD pattern for NCACB after annealing at 1150 °C for 1 h; (B) EDS Mapping for NCACB after annealing at 1150 °C for 1 h.

microstructure design over the range (blue ellipse) of high strength and high ductility, especially the HL-HEA sample. In the following part, a study is carried out to specifically investigate deformation mechanisms of the HL-HEA, which can help explain its exceptional properties.

Heterogeneous lamella structured materials overcome the strength-ductility trade-off by means of enhancing the strain hardening ability [41] to avert early necking [42]. At the onset of plasticity, coarse grained lamellae yield first, while the fine grained lamellae remain mostly elastic; this is effectively a local Hall-Petch phenomenon [43]. Since, due to higher resolved shear stresses generated by more dislocation pile-ups over a larger grain diameter [44], coarse-grained lamellae reach the critical resolved shear stress faster than the fine-grained regions. Thus, coarse grains will eventually carry more plastic strain than fine grains in the later deformation stages, i.e. strain partitioning. To maintain compatibility across the CG-(soft)/FG-(hard) interface under the rigid plastic material assumption, the coarse grains must deform heterogeneously to avoid formation of voids and material overlap [45], which generates strain gradients [46]. Furthermore, accommodation of the plastic strain gradient is through multiplication and storage of geometrically necessary dislocations (GND) [47–49] instead of the more randomly distributed statistically stored dislocations (SSD) [45]. Pile-ups of GNDs across the microstructure are believed to be responsible for generating long-range back-stresses that resists forward dislocation motion and leads to the Bauschinger effect and pronounced strain hardening [12]. Loading-unloading-reloading (LUR) cyclic tensile tests are carried out to calculate the back-stress as shown in Fig. 4(C)–(D). All the LUR cyclic tensile tests results can be found in Fig. S7. Details of back-stress calculation can be referred to Ref. [12]. However, very few

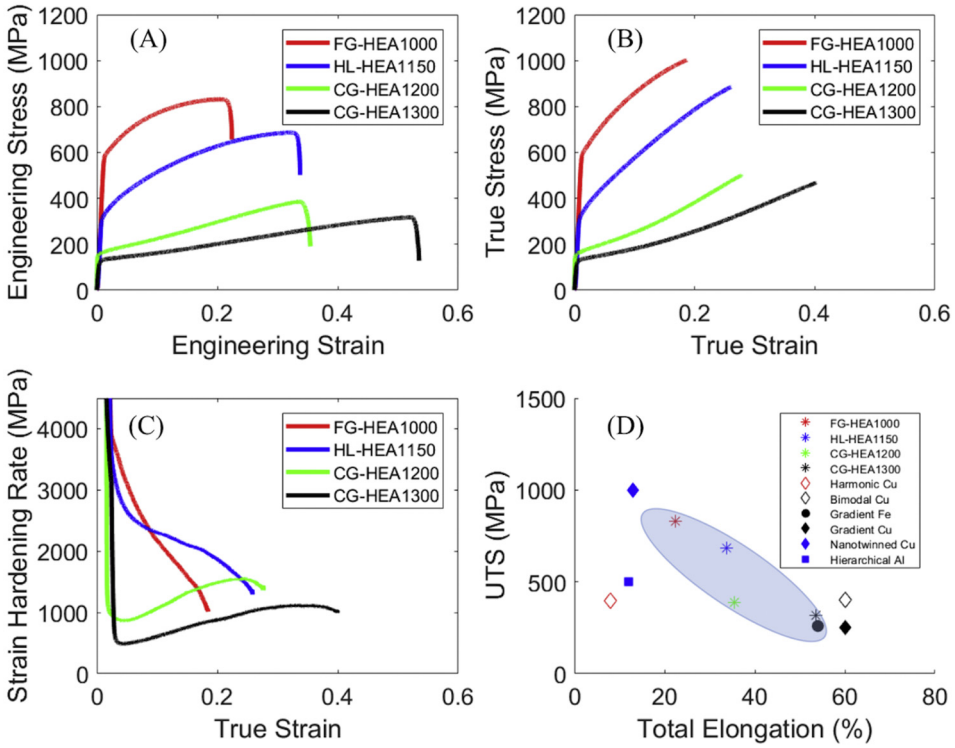

Fig. 3. Tensile behavior of NCACB with four different grain structures. (A) Tensile engineering stress-strain curves; (B) tensile true stress-strain curves; (C) strain hardening rate curves; (D) comparison of mechanical properties between HL-NCACB-HEA and other materials with similar structures (harmonic Cu [55], bimodal Cu [21], gradient Fe [12], gradient Cu [20], nanotwinned Cu [56] and hierarchical Al [22]). (For interpretation of the references to color in this figure legend, the reader is referred to the web version of this article.)

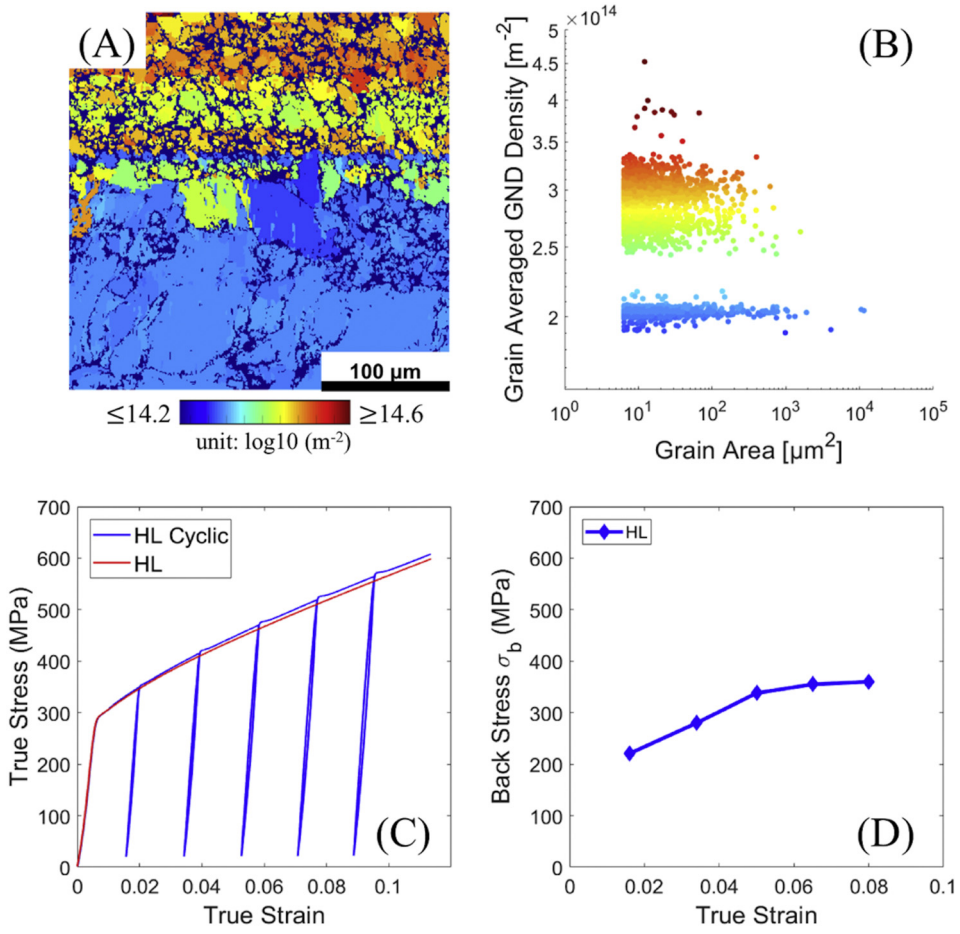

Fig. 4. (A) Grain average GND density map in logarithmic scale (color bar: 14.2–14.6 [unit: log10 (m^{-2})]); (B) grain average GND density (m^{-2}) plotted against grain area (μm^2) with each data point colored according to the order of magnitude of grain average GND density (color bar: 14.2–14.6 [unit: log10 (m^{-2})]); (C) true stress-strain curves for LUR cyclic tensile tests of HL-1150; (D) back-stress of HL-1150. (For interpretation of the references to color in this figure legend, the reader is referred to the web version of this article.)

studies have been carried out to measure the distribution of the GND density and relate the distribution of GNDs to the heterogeneous microstructure. Hence, a quantitative analysis of the GND distribution will not only provide insight into the failure of this material, but also experimentally verify the local back-stress strengthening mechanism. Recent advances in EBSD allow fast and accurate characterization of many aspects of materials, e.g. crystal orientation, texture, microstructure, etc. [50,51]. Moreover, the EBSD-based GND density measurement is established based on crystal orientation data [52,53]. By constructing the Nye dislocation density tensor using measured disorientation gradients, dislocation density values related to a specific type of dislocation are computed. In this study, the typical ⟨110⟩{111} dislocation configurations in FCC are assumed: 6 screw and 12 edge dislocations [26,49]. Using the EBSD orientation data obtained from Supplementary Fig. S5 (E), the GND density map of a CG-FG interface near the point of failure is plotted as shown in Supplementary Fig. S6(A). The logarithmic color scale utilized in plotting the GND map reveals notable heterogeneity of deformation across the CG-FG interface, particularly in the coarse-grained lamella. GND hot spots are most commonly found near geometric constraints such as triple junctions and grain boundaries. The step size of 0.8 μm establishes a noise floor to be around 1.2×10^{13} dislocations/m^2, which is below the majority of the data points, as shown by the distribution plot in Supplementary Fig. S6(B). The area fraction distribution is a slightly left-skewed normal distribution due to the sampling of very few large grains with large GND 'cold-spots' in the grain interiors. To probe the dependence of the GND density on the size of the individual grains, grains are first indexed using a misorientation threshold of 5° to separate them from the deformation texture. Next, the area of each grain is approximated by the number of pixels of a given grain times the size of the pixel in square micrometers. The grain average GND density is readily computed as the geometric mean of the GND density values obtained from each pixel of a specified grain. In Fig. 4(B), it can be found that the grain average GND density versus grain area data is separated into two distinct regions above and below ~2.3×10^{14} dislocations/m^2. Then, each data point in Fig. 4 (B) has its grain average GND density value distributed over the corresponding grain and produces a map as in Fig. 4(A). It can be found that the high-density data (>2.3×10^{14} m^{-2}) lies primarily within the FG region, whereas the low-density data (<2.3×10^{14} m^{-2}) resides mostly in the CG region. This means that the residual stresses are overall higher in the FG region and on average lower in the CG region. Therefore, potential failure is more likely to initiate from the FG region and then traverse through the CG-FG interface, and eventually lead to failure of the entire sample. Most interesting in this analysis is the discovery of a layer of high-density grains immediately adjacent to the CG side of the CG-FG interface, and a layer of low-density grains on the FG side of the CG-FG interface. The high-density layer is the 'compatibility layer', which restores compatibility in plastic strain near the CG-FG interface through generating large amount of GNDs. In other words, the CG region homogenizes the otherwise highly heterogeneous plastic strain distribution in the FG region by activating multi-slip along the interface [54]. Since the 'compatibility layer' carries more plastic strain gradients on the interface, this results in the formation of a low-density 'transition layer' with relatively uniform plastic strain into the high residual stress FG region. A more comprehensive study regarding generation of back-stress would involve plastic strain analysis using DIC coupled with

crystal plasticity finite element methods, which is the subject of future work.

In summary, a precipitation-controlled method for tuning the microstructure of non-equiatomic FeNiCoAlCrB (NCACB) high entropy alloy is proposed, which provides an opportunity to modify mechanical properties within a strength and ductility window perhaps more effectively than a large number of existing metals and alloys. In this study, the heterogeneous lamella HEA has demonstrated better mechanical properties over fine grained and coarse grained HEAs due to the back-stress strengthening mechanism.

Acknowledgement

We would like to thank Zezhou Li, Sumin Shin, Sabine Faulhaber, Wayne Neilson and Mojtaba Samiee for help on experiments.

Appendix A. Supplementary data

Supplementary data to this article can be found online at https://doi.org/10.1016/j.scriptamat.2018.05.020.

References

[1] J.W. Yeh, S.K. Chen, S.J. Lin, J.Y. Gan, T.S. Chin, T.T. Shun, C.H. Tsau, S.Y. Chang, Adv. Eng. Mater. 6 (5) (2004) 299.
[2] B. Cantor, I. Chang, P. Knight, A. Vincent, Mater. Sci. Eng. A 375 (2004) 213.
[3] Y. Zhang, T.T. Zuo, Z. Tang, M.C. Gao, K.A. Dahmen, P.K. Liaw, Z.P. Lu, Prog. Mater. Sci. 61 (2014) 1.
[4] B. Gludovatz, A. Hohenwarter, D. Catoor, E.H. Chang, E.P. George, R.O. Ritchie, Science 345 (6201) (2014) 1153.
[5] D. Miracle, O. Senkov, Acta Mater. 122 (2017) 448.
[6] Z. Li, K.G. Pradeep, Y. Deng, D. Raabe, C.C. Tasan, Nature 534 (7606) (2016) 227.
[7] F. Otto, A. Dlouhý, K.G. Pradeep, M. Kuběnová, D. Raabe, G. Eggeler, E.P. George, Acta Mater. 112 (2016) 40.
[8] C.C. Tasan, Y. Deng, K.G. Pradeep, M. Yao, H. Springer, D. Raabe, JOM 66 (10) (2014) 1993.
[9] Z. Li, C.C. Tasan, K.G. Pradeep, D. Raabe, Acta Mater. 131 (2017) 323.
[10] M. Yao, K. Pradeep, C. Tasan, D. Raabe, Scr. Mater. 72 (2014) 5.
[11] E. Ma, T. Zhu, Mater. Today 20 (6) (2017) 323.
[12] X. Wu, M. Yang, F. Yuan, G. Wu, Y. Wei, X. Huang, Y. Zhu, Proc. Natl. Acad. Sci. 112 (47) (2015) 14501.
[13] X. Wu, P. Jiang, L. Chen, F. Yuan, Y.T. Zhu, Proc. Natl. Acad. Sci. 111 (20) (2014) 7197.
[14] A. Magee, L. Ladani, T.D. Topping, E.J. Lavernia, Acta Mater. 60 (16) (2012) 5838.
[15] D. Witkin, Z. Lee, R. Rodriguez, S. Nutt, E. Lavernia, Scr. Mater. 49 (4) (2003) 297.
[16] H. Azizi-Alizamini, M. Militzer, W. Poole, Scr. Mater. 57 (12) (2007) 1065.
[17] Z. Zhang, S.K. Vajpai, D. Orlov, K. Ameyama, Mater. Sci. Eng. A 598 (2014) 106.
[18] G. Fan, H. Choo, P. Liaw, E. Lavernia, Acta Mater. 54 (7) (2006) 1759.
[19] X. Wu, M. Yang, F. Yuan, L. Chen, Y. Zhu, Acta Mater. 112 (2016) 337.
[20] T. Fang, W. Li, N. Tao, K. Lu, Science 331 (6024) (2011) 1587.
[21] Y. Wang, M. Chen, F. Zhou, E. Ma, Nature 419 (6910) (2002) 912.
[22] P.V. Liddicoat, X.-Z. Liao, Y. Zhao, Y. Zhu, M.Y. Murashkin, E.J. Lavernia, R.Z. Valiev, S.P. Ringer, Nat. Commun. 1 (2010) 63.
[23] S. Guo, C. Ng, J. Lu, C. Liu, J. Appl. Phys. 109 (10) (2011) 103505.
[24] Y. Zhang, Y.J. Zhou, J.P. Lin, G.L. Chen, P.K. Liaw, Adv. Eng. Mater. 10 (6) (2008) 534.
[25] C. Zhu, V. Livescu, T. Harrington, O. Dippo, G.T. Gray III, K.S. Vecchio, Int. J. Plast. 92 (2017) 148.
[26] C. Zhu, T. Harrington, V. Livescu, G.T. Gray III, K.S. Vecchio, Acta Mater. 118 (2016) 383.
[27] H. Chen, A. Godfrey, N. Hansen, J. Xie, Q. Liu, Mater. Sci. Eng. A 483 (2008) 157.
[28] D.A. Hughes, N. Hansen, Acta Mater. 48 (11) (2000) 2985.
[29] S. Bellier, R. Doherty, Acta Metall. 25 (5) (1977) 521.
[30] G. Rosen, D.J. Jensen, D. Hughes, N. Hansen, Acta Metall. 43 (7) (1995) 2563.
[31] J. Zhang, M. Ma, W. Liu, Mater. Sci. Eng. A 690 (2017) 233.
[32] N. Hansen, D. Juul Jensen, Mater. Sci. Technol. 27 (8) (2011) 1229.
[33] B. Bay, N. Hansen, D. Hughes, D. Kuhlmann-Wilsdorf, Acta Metall. 40 (2) (1992) 205.
[34] F. Humphreys, Acta Metall. 25 (11) (1977) 1323.
[35] O. Mishin, A. Godfrey, D.J. Jensen, N. Hansen, Acta Mater. 61 (14) (2013) 5354.
[36] Y. Sutou, N. Koeda, T. Omori, R. Kainuma, K. Ishida, Acta Mater. 57 (19) (2009) 5759.
[37] Y. Sutou, T. Omori, K. Yamauchi, N. Ono, R. Kainuma, K. Ishida, Acta Mater. 53 (15) (2005) 4121.
[38] Y. Chen, X. Zhang, D.C. Dunand, C.A. Schuh, Appl. Phys. Lett. 95 (17) (2009), 171906.
.
[39] S.M. Ueland, Y. Chen, C.A. Schuh, Adv. Funct. Mater. 22 (10) (2012) 2094.
[40] Y. Chen, C.A. Schuh, Acta Mater. 59 (2) (2011) 537.
[41] X. Wu, Y. Zhu, Math. Res. Lett. 5 (8) (2017) 527.
[42] E. Hart, Acta Metall. 15 (2) (1967) 351.
[43] N. Hansen, Scr. Mater. 51 (8) (2004) 801.
[44] J. Eshelby, F. Frank, F. Nabarro, Philos. Mag. 42 (327) (1951) 351.
[45] M. Ashby, Philos. Mag. 21 (170) (1970) 399.
[46] H.K. Park, K. Ameyama, J. Yoo, H. Hwang, H.S. Kim, Math. Res. Lett. 6 (5) (2018) 261.
[47] J.F. Nye, Acta Metall. 1 (2) (1953) 153.
[48] E. Kroner, Continuum Theory of Dislocations and Self-stresses, Springer, 1958.
[49] E. Demir, D. Raabe, N. Zaafarani, S. Zaefferer, Acta Mater. 57 (2) (2009) 559.
[50] K. Lassen, Mater. Sci. Technol. 12 (10) (1996) 837.
[51] B.L. Adams, S.I. Wright, K. Kunze, Metall. Mater. Trans. A 24 (4) (1993) 819.
[52] S. Sun, B. Adams, W. King, Philos. Mag. A 80 (1) (2000) 9.
[53] B. El-Dasher, B. Adams, A. Rollett, Scr. Mater. 48 (2) (2003) 141.
[54] R. Yuan, I.J. Beyerlein, C. Zhou, Mater. Res. Lett. 5 (4) (2017) 251.
[55] D. Orlov, H. Fujiwara, K. Ameyama, Mater. Trans. 54 (9) (2013) 1549.
[56] L. Lu, Y. Shen, X. Chen, L. Qian, K. Lu, Science 304 (5669) (2004) 422.